Raman Scattering Investigation of Structural Transition in Ca5Ir3012

doi: https://doi.org/10.7566/JPSJ.89.054602

Raman Scattering Investigation of Structural Transition in $Ca_5Ir_3O_{12}$

Takumi Hasegawa[1*], Wataru Yoshida [2†], Kazuma Nakamura[2], Norio Ogita[1] and Kazuyuki Matsuhira[2]

[1]*Graduate School of Integrated Arts and Sciences, Hiroshima University, 1-7-1 Kagamiyama, Higashi-Hiroshima 739-8521, Japan*

[2]*Faculty of Engineering, Kyushu Institute of Technology, Kitakyushu 804-8550, Japan*

We report a study of the second-order phase transition at 105 K in the geometrically frustrated iridate $Ca_5Ir_3O_{12}$ using a Raman scattering method. The Raman scattering spectra of a single crystal were measured from 4 K to room temperature. *Ab initio* phonon calculations that consider the spin-orbit interaction were also conducted and compared with the experimental spectra. Agreement between the theoretical and experimental results at room temperature is reasonably good. At room temperature, $6A_1' + 9\,E' + 5E''$ were assigned among the Raman active modes, $6A_1' + 13E' + 6E''$, based on the reported $P\bar{6}2m$ crystal structure. Below T_s, 23 additional peaks were observed, suggesting the appearance of a superlattice structure. The polarization dependence of Raman spectra below T_s indicates the existence of $\bar{6}$ symmetry. We observed at least one additional mode as a broad weak-intensity peak at temperatures higher than T_s. This suggests possible local distortion around the Ir ions, which would be expected for Ir ions with mixed valence states.

1. Introduction

Recently, Ir oxides have been actively researched owing to their attractive magnetic and transport properties caused by strong spin-orbit interaction (SOI).[1–5] In particular, in the case of Ir^{4+} ($5d^5$), the strong SOI splits the six-fold degenerate t_{2g} states into the occupied $J_{eff} = 3/2$ and half-occupied $J_{eff} = 1/2$ states.[6] The half-occupied $J_{eff} = 1/2$ bands are narrower than the width of the entire t_{2g} band formed in the absence of SOI. Consequently, a Mott-insulating state is realized even when moderate correlations exist between the $5d$ electrons.

$Ca_5Ir_3O_{12}$ has a hexagonal structure with a noncentrosymmetric space group of $P\bar{6}2m$

*E-mail address: hase@hiroshima-u.ac.jp

†present address: Nara Institute of Science and Technology

(No. 189). In the crystal structure, one-dimensional chains of the edge-sharing IrO_6 octahedra form a triangular lattice in the c-plane. $Ca_5Ir_3O_{12}$ contains a mixed valance state of Ir^{4+} and Ir^{5+}, with the average valence of the Ir ions being +4.67; hence, a metallic state is expected in the unfilled bands. However, $Ca_5Ir_3O_{12}$ exhibits semiconducting conductivity.[7)] In the recent past, it was discovered that, along the c-axis, $Ca_5Ir_3O_{12}$ shows nonlinear conductivity below 300 K[8)] and antiferromagnetic (AFM) ordering below the Néel temperature T_N = 7.8 K.[7,9–11)] In addition, $Ca_5Ir_3O_{12}$ exhibits a second-order phase transition at T_s = 105 K, where the specific heat exhibits sharply anomalous behavior and the electrical resistivity shows a sharp bending upward. As these structural and magnetic transitions have not been confirmed by X-ray diffraction, neutron scattering, or μSR experiments in the powder samples, the origin of the phase transition at 105 K is presently unclear[7,11)] and is a problem that needs to be solved for this compound. As described above, the behavior of $Ca_5Ir_3O_{12}$ is complex because Ir exists as a mixture of the valence states Ir^{4+} and Ir^{5+} in a ratio of 1 : 2 based on the averaged valence of the Ir ion. This situation can lead to the geometric frustration of electric charge on both the triangular lattice in the c-plane and in the 1D chains along the c-axis. We could speculate that the phase transition at 105 K has its origin in charge ordering of Ir the ions, although, in the case of charge ordering, a structural change is observed in many transition metal oxides.[12)]

In this paper, we report the result of Raman scattering experiments on a single crystal of $Ca_5Ir_3O_{12}$. In addition, we present the phonon frequencies and atomic displacements obtained by *ab initio* density functional calculations.

2. Methods

Single crystals of $Ca_5Ir_3O_{12}$ were grown by the $CaCl_2$ flux method as reported previously.[8)] We will comment on sample quality of single crystal used in this experiment. In the case of polycrystalline samples, the phase transition at 105 K is observed in the electrical resistivity of all the samples we synthesized thus far. On the other hand, for single crystal samples grown by the $CaCl_2$ flux method using the polycrystal, sample dependence on the phase transition at 105 K is observed. However, single crystal samples that exhibit no anomaly in their resistivity at the phase transition also exist. The Raman scattering measurements reported in this paper were performed using a single crystal for which the phase transition at 105 K was observed. In addition, in the preliminary experiments, we carried out Raman scattering measurements on a polycrystalline sample. Our results confirmed that the Raman scattering spectrum of a polycrystalline sample can be explained by the spectrum we

obtained for the single crystal. Therefore, we can conclude that the particular single crystal is of high quality.

Raman scattering experiments were performed using a high-quality single crystal. The shape is a hexagonal prism elongated along the c-axis. Its side surface is perpendicular to the a-axis. Raman spectra were measured by using quasi-backscattering geometry on this surface, which was polished beforehand. Raman scattering was excited with a 561.4 nm solid-state laser (Spectra Physics, Excelsior ONE), with power of 10 mW before the cryostat. The scattered light was dispersed by a triple monochrometer (JASCO, NR-1800), and was accumulated on a liquid-N_2 cooled CCD (Princeton Instruments Inc., LN/CCD-1100PB). The measurements at low temperatures were obtained by using a cryostat cooled by a GM cryocooler (SHI SRDK-205). The energy of the measured spectra was corrected by using the natural emission lines of a He-Ne laser in comparison with the reported wavelengths.[13] Polarization of the incident and scattered light were written as $(\mathbf{i}, \mathbf{s})$, where the first and second vectors in the bracket refer to the directions of the polarization direction of the incident and the scattered light, respectively. The polarization directions of the light were restricted to the c or b^* direction, where b^* is the reciprocal vector perpendicular to the c and a axes. We measured the (c, c), (b^*, c), and (b^*, b^*) polarization geometries.

Density functional calculations with plane-wave basis sets were performed using the xTAPP code,[14] where the ultrasoft pseudopotential[15,16] and generalized gradient approximation (GGA) of the exchange correlation potential were employed.[17] The cutoff energies in the wavefunction and charge densities were 64 and 900 Ry, respectively, and SOI was explicitly considered. The ultrasoft pseudopotentials were updated from those that were previously reported[8] and confirm that our pseudopotential reproduces the band structures reported before.[8] We studied the effects of SOI by conducting the usual GGA calculation and by comparing it with the result including SOI. Hereafter, we refer to the former situation as GGA and to the latter as SO-GGA. The atomic and lattice parameters were optimized with $8 \times 8 \times 8$ k-point sampling, and we found that our density functional calculation reproduces the experimental crystal structure quite well. Phonon calculations with a frozen phonon approximation were performed using the PHONOPY package,[18–20] and a $1 \times 1 \times 3$ supercell and $11 \times 11 \times 11$ k-point sampling were employed. It is to be noted that the phonon calculations were performed by considering the original symmetry based on the point group $\bar{6}2m$. The phonon frequencies at $\mathbf{q} = \mathbf{0}$ and their atomic displacements were evaluated and compared with the present Raman spectra.

3. Results

3.1 Crystal Structure

At room temperature, the crystal structure of $Ca_5Ir_3O_{12}$ belongs to the space group $P\bar{6}2m$, as shown in Fig. 1. There are five atomic positions: Ca1 at (1/3, 2/3, 1/2), Ca2 at (x_{Ca2}, 0, 1/2), Ir at (x_{Ir}, 0, 0), O1 at (x_{O1}, 0, 1/2), O2 at (x_{O2}, 0, 1/2), and O3 at (x_{O3}, y_{O3}, 0).[7] Since there is only one Ir site, a charge-ordered state must lower the symmetry. Table I compares the experimental and theoretical structural data. Our *ab initio* results reasonably reproduce the experimental data within 3 %. We found the total energy for the SO-GGA to be stable by 0.869 [eV/cell] compared to that of the GGA.

3.2 Ab initio Phonon Calculations

Figures 2(a) and 2(b) show our calculated phonon dispersions with and without SOI, respectively, and Fig. 2(c) compares the two densities of states. Considering the SOI, the density of state is slightly red-shifted as a whole, and seems to exhibit behavior similar to that of simple face-centered cubic Pb,[21] even though the present system is more complicated. The zero-point free energy due to the lattice vibration is found to be basically the same between the two, i.e., 1.285 [eV/cell] for SO-GGA and 1.307 [eV/cell] for GGA. The SO-GGA phonon system is slightly more stable by 0.02 [eV/cell] compared to the GGA system. We also calculated the vibrational modes at the Γ point, and used these modes to analyze the Raman spectra at room temperature (see Sec. 3.4).

3.3 Raman Spectra and Assignment at Room Temperature

Before discussing the experimental Raman spectra, we briefly describe the factor group analysis to determine the Raman activity. The phonon modes at $\mathbf{q} = \mathbf{0}$ are decomposed into the irreducible representations of the point group $\bar{6}2m$ as

$$6A_1' + 6A_2' + 2A_1'' + 6A_2'' + 14E' + 6E''. \tag{1}$$

In these modes, $A_2'' + E'$ are acoustic modes, and the Raman active modes are $6A_1' + 13E' + 6E''$. In this crystal structure, all atoms are located on the mirror plane perpendicular to the c-axis. In this case, any vibration along the c-axis belongs to A_1'', A_2'', or E''. The other A_1', A_2', and E' modes have displacements of atoms in the c-plane. The A_1' modes can be observed on the (c, c) and (b^*, b^*) spectra, the E' modes on the (b^*, b^*) spectra, and the E'' modes on the (b^*, c) spectra. Figure 3(a) shows the (c, c), (b^*, b^*), and (b^*, c) spectra at room temperature. Because of the weaker intensity of the (b^*, b^*) and (b^*, c) spectra relative to that of the (c, c) spectrum, magnified spectra are also shown in Fig. 3(b).

The (c, c) spectrum, which only displays the A_1' modes, is characterized by five prominent peaks. Since the shape of the peak centered at 550 cm^{-1} is asymmetric, we recognize it as a superposition of two peaks. This assignment is consistent with the calculated results, which are shown in Fig. 3(a) by using vertical lines and triangles. Therefore, we assigned the six A_1' modes as shown by the arrows in Fig. 3(a). These energies are estimated by fitting the Lorentzian curve, and are listed in Table II.

The spectrum of (b^*, c) exhibits five peaks, as shown in Fig. 3(b), and are assigned to the E″ modes. Considering that six E″ modes exist, one of the E″ modes was not displayed. In comparison with the calculated results (see Table II and Fig. 3(b)), the energy of the missing E″(4) mode is expected to be approximately 380 cm^{-1}.

The spectrum of (b^*, b^*) displays the A_1' and E′ modes. The A_1' modes have already been assigned in (c, c), and are indicated by the vertical arrows in Fig. 3(b). The four peaks in the (b^*, b^*) spectrum are assigned to $A_1'(1)$, $A_1'(2)$, $A_1'(3)$, and $A_1'(6)$. The other eight peaks are assigned to E′ modes. We labeled these peaks by comparing the energy with the calculated energies. It is necessary to comment on the assignment of E′(4) at 231 cm^{-1}, E′(12) at 562 cm^{-1}, and E′(13) at 615 cm^{-1}. The peak at approximately 230 cm^{-1} is slightly asymmetric. The asymmetry becomes clear at 110 K (see the inset of Fig. 4). Therefore, we considered it to consist of the two peaks of $A_1'(2)$ and E′(4). The peak at 560 cm^{-1} might be $A_1'(5)$. However, this peak is not coincident to the peak of $A_1'(5)$ at 110 K, as indicated in Fig. 4 by the vertical line. Because it must be an E′ mode, it is assigned to E′(12). The shoulder beside the large peak of $A_1'(6)$ near 660 cm^{-1} is ambiguous at room temperature, but becomes clearly resolved at 110 K. This shoulder was assigned to E′(13).

3.4 Comparison between Experiment and Theory

The observed energies and their assignments are listed in Table II. We assigned $6A_1'$ + 9E′ + 5E″ to the Raman active $6A_1'$ + 13E′ + 6E″ modes. The result is consistent with the reported crystal structure. Therefore, a charge-ordered state was not detected at room temperature, although semiconducting conductivity was reported at room temperature.[7)]

The calculated phonon energies of SO-GGA and GGA are also listed in Table II for both the Raman active and Raman inactive modes. The difference between the observed and calculated energies is lower than 10 % for SO-GGA, and 11 % for GGA, while the difference between the two calculations is only 5 %. Therefore, we can conclude that both calculations coincide with the experimental result to the same extent. Hereafter, we discuss the experimental result with comparison to SO-GGA. This coincidence between the experiment and the

calculated results is not evident because the calculated electronic state is metallic. It should be noted that the observed conductivity is that of a semiconductor. This coincidence in the phonon energies leads to two possibilities. One is that the origin of the change in the conduction does not largely affect the phonon energies at $\mathbf{q} = \mathbf{0}$. As discussed in sec. 4.1, the present result suggests the possibility of a super-lattice structure. Therefore, the phonon modes at certain characteristic $\mathbf{q}$ might deviate from the calculated values. The other is that the difference in the electronic state between the calculated metal and the actual semiconductor is small. Only the electrons close to the Fermi energy are rearranged to open a gap such that its effect on the phonon energies might be small.

3.5 Changes in Spectra at Low Temperatures

The Raman spectra at 110 K and at 4 K are shown in Fig. 4 and Fig. 5, respectively. Since the transition temperature T_s is 105 K, the spectra in Fig. 4 are those above T_s. Without a phase transition, decreasing the temperature has the effect of decreasing the line-width and increasing the energy. The changes in the (b^*, b^*) and (b^*, c) spectra at 110 K were those that were expected, except that some weak-intensity peaks were not observed. However, the (c, c) spectrum at 110 K contains a clear additional peak at approximately 440 cm^{-1} and another peak near 550 cm^{-1}, which is observed as a peak with a rounded top. This is an unexpected result, because no phase transition has been reported between 105 K and room temperature. The additional peaks suggest the occurrence of a structural change in this temperature range. In sec. 3.6, we discuss their temperature dependence.

At 4 K, many additional peaks were found as indicated by the vertical lines in Fig. 5. This is clear evidence of structural change from the room temperature structure. It is noteworthy that each of the additional peaks is observed on only one spectrum. For example, all the additional peaks found on the (b^*, b^*) spectrum were not observed on the (b^*, c) spectrum, and vice versa. Based on this finding, we can classify the additional peaks in the same manner as those at room temperature. Therefore, according to the irreducible representations of $\bar{6}2m$, we refer to the additional peaks on the (c, c) spectra as $\mathrm{A}'_{1\mathrm{LT}}$, those on the (b^*, b^*) spectra as $\mathrm{E}'_{\mathrm{LT}}$, and that on the (b^*, c) spectra as $\mathrm{E}''_{\mathrm{LT}}$, tentatively. Although $\mathrm{A}'_{1\mathrm{LT}}$ could possibly exist on (b^*, b^*) according to the point group $\bar{6}2m$, no such peak appears on the (b^*, b^*) spectrum with the same energy as $\mathrm{A}'_{1\mathrm{LT}}$ within the experimental accuracy (approximately 0.7 cm^{-1}). The energies of the observed modes are listed in Table III. In this estimation of the energies, we should mention the decomposition of the complicated spectrum in the vicinity of 550 cm^{-1} on the (c, c) spectrum. This spectrum is reproduced by five Lorentz peaks as shown in Fig. 6.

Next, we discuss the point group of the crystal structure at 4 K. The observed polarization dependence can be explained by the point group $\bar{6}$, which contains four irreducible representations, A′, A″, E′, and E″. The corresponding relations are the following: A'_1 and A'_2 in $\bar{6}2m$ become A′ in $\bar{6}$, A''_1 and A''_2 in $\bar{6}2m$ are A″ in $\bar{6}$, and E′ and E″ change in neither of the point groups. If $\bar{6}$ is broken, E′ and E″ is not distinguished. Then, a mode can be observed in the (b^*, b^*) and (b^*, c) geometries. Therefore, we can infer the existence of $\bar{6}$ from the polarization dependence. Only the fact that the peak at 660.9 cm^{-1} was found on the (b^*, c) spectrum may be evidence that $\bar{6}$ is breaking. This would occur the $E'_{LT}(12)$ mode, which is forbidden in the (b^*, c) geometry, if $\bar{6}$ is conserved. The intensity on the (b^*, c) spectrum is relatively weak, i.e., the ratio of the intensity on the (b^*, c) spectrum to that on the (b^*, b^*) spectrum is approximately 0.01. This peak has also been observed in some (b^*, c) spectra above T_s at various intensities. We consider this peak to be the results of misalignment of the crystal, e.g., that the incident laser focused partially on a side, edge, or step of the surface. Therefore, we conclude that the breaking of $\bar{6}$ is not detected at 4 K.

Another way to probe the breaking of the $\bar{6}2m$ symmetry would be to attempt to detect the splitting of the doubly degenerate E′ and E″ modes. Strictly speaking, this would confirm the existence of the 3-fold symmetry. At 4 K, some additional peaks were observed with energy close to that of the E′ modes. These peaks might be considered to have split from the E′ mode. However, as shown in sec. 3.7, these peaks appear with increasing intensity and are not moved from the E′ mode as would be expected for a splitting. Since the large line width obscures possible splitting, it is noteworthy to discuss the narrowest peak of the E′ and E″ modes. The E″(1) at 84 cm^{-1} is the narrowest, i.e., 3.2 cm^{-1} full-width at half-maximum (FWHM). This width closely approximates the resolution of the monochrometer, and the observed width is independent of temperature. Namely, this mode did not split at the resolution limit. This mode is the vibration of Ir-O chains along the c-axis. The degeneracy of this mode prevents the 3-fold symmetry from breaking. Therefore, we conclude that the 3-fold symmetry is conserved at 4 K.

3.6 Temperature Dependence above 105 K

As shown in Fig. 4, an additional peak, $A'_{1LT}(6)$, at approximately 420 cm^{-1} was observed at 110 K, which is above T_s. This might imply another transition above T_s. To clarify the temperature above which the peak vanishes, we measured the temperature dependence of the (c, c) spectrum above T_s. Figure 7 shows the (c, c) spectrum from 110 K to 200 K. At high temperatures, the peak of $A'_{1LT}(6)$ broadens and weakens. It is difficult to discuss the

existence of such a broad peak, because it is likely to be accidentally detected beside the well-resolved peak of $A_1'(3)$. Actually, we can extract $A_{1LT}'(6)$ even at room temperature by applying two Lorentzian peaks at approximately 450 cm^{-1}. The extracted peaks are shown in Fig. 7. To discuss the intensity of the peaks, we define I_0 as the integrated intensity corrected by the Bose factor $1/(1 - \exp(-\hbar\omega/k_B T))$, where ω is the frequency of the corresponding vibrational mode. The ratio of I_0 of $A_{1LT}'(6)$ to that of $A_1'(3)$ is shown in Fig. 8. Its intensity decreases gradually with increasing temperature. Therefore, we consider the origin of this additional peak to be a local structural distortion rather than a transition.

The temperature dependence of the energies of the $A_{1LT}'(6)$ mode and the $6A_1'$ modes are shown in Figs. 8 and 9, respectively. The energy of $A_1'(1)$ is almost independent of temperature above T_s. The other A_1' modes become hard at low temperatures, as is usually observed for phonon modes. The energy of $A_{1LT}'(6)$ decreases near T_s, although the uncertainty associated with this mode makes it difficult to discuss the temperature dependence above T_s.

The FWHM of the $A_{1LT}'(6)$ mode and the $6A_1'$ modes are also shown in Figs. 8 and 9, respectively. The width of the $A_1'(1)$ mode is the same as the resolution width of the monochrometer, which is approximately 3.2 cm^{-1}. Line widths generally decrease at low temperatures owing to their increasing lifetime. However, the width of $A_1'(4)$ at approximately 545 cm^{-1} was observed to increase with decreasing temperature. The line shape of this mode has a rounded top at 110 K, and is not well expressed by one Lorentz curve. This indicates that this peak consists of two modes, $A_1'(4)$ and $A_{1LT}'(9)$ even above T_s. We should consider that the $A_{1LT}'(9)$ at 560 cm^{-1} was observed above T_s, in addition to the $A_{1LT}'(6)$ at 420 cm^{-1}.

The width of $A_1'(5)$ rapidly decreases below 150 K, which is higher than T_s. If another transition existed, the transition would occur at approximately 150 K. However, none of the other modes show anomalous behavior near 150 K. Since $A_{1LT}'(6)$ was observed above 150 K, an additional transition would be required to explain the appearance of this mode. Instead of such a transition, the observations could be explained by local distortion, as suggested by the existence of the $A_{1LT}'(6)$ and $A_{1LT}'(9)$ modes above T_s. The distortion would fluctuate at high temperatures and the fluctuation would become slower and weaker with decreasing temperature. If the fluctuation were to scatter the $A_1'(5)$ mode effectively, the width of $A_1'(5)$ would be proportional to the amplitude of the fluctuation. Therefore, the observed decrease in the width is interpreted to mean that the fluctuation is suppressed below 150 K.

3.7 Temperature dependence below 105 K

The (c, c) spectra below T_s are shown in Fig. 10. The spectral changes are consistent with the transition at T_s. Below T_s, the intensity of the additional peaks increases and the line widths of the A_1' modes decrease. The intensity I_0 of the A_1' modes is almost independent of temperature even below T_s. It should be noted that I_0 of the $A_{1LT}'(6)$ mode decreases below T_s, as shown in Fig. 8. This behavior is opposite to that expected for additional peaks. This anomaly is probably caused by part of the broad peak at approximately 420 cm^{-1} being missing below T_s. A broad weak-intensity peak is noticeable even below T_s as shown in Fig. 5 in addition to the narrower $A_{1LT}'(6)$ peak. This means the local distortions partially acquire a long lifetime such that it was observed as the sharp $A_{1LT}'(6)$ peak below T_s, whereas the remainder continue to have a short lifetime such that the peak was observed as a broad spectrum. This broad spectrum was not included in this analysis. This is considered to be the reason for the decrease in intensity.

In terms of the complicated peaks surrounding 550 cm^{-1}, although it is difficult to estimate individual I_0 values, the I_0 of $A_{1LT}'(8)$ at 481 cm^{-1} increases with increasing temperature. The summation of I_0 for the other four modes is independent of temperature. These facts indicate that $A_{1LT}'(8)$ is an additional peak below T_s and $A_{1LT}'(10)$ at 590 cm^{-1} might exist above T_s in addition to the $A_{1LT}'(9)$ mode.

The energy of the A_1' modes show no anomaly at T_s as shown in Fig. 9. For $A_1'(4)$, a gap is shown at 110 K. This is because the process to extract the energies is different: five Lorentzian peaks are used below 110 K, whereas two Lorentzian peaks are adopted above 110 K. On the other hand, the line width below T_s is clearly found to decrease for $A_1'(4)$. This decrease is also found for $A_{1LT}'(6)$ as shown in Fig. 8. The decrease in the line width of these modes means that the fluctuation of the structural transition either weakens or ceases to exist below T_s.

The (b^*, b^*) spectra are shown in Fig. 11. The E′ modes in (b^*, b^*) are doubly degenerate, and are split into two peaks if the 3-fold axis is lost below T_s. There are five E′ modes, which have a side peak at 4 K. They are E′(6) at 326 cm^{-1}, E′(7) at 390 cm^{-1}, E′(9) at 478 cm^{-1}, E′(10) at 520 cm^{-1}, and E′(12) at 571 cm^{-1}. If the E′ modes were to split into two peaks, one peak would clearly separate from the other, and their intensities would not change largely. However, for all of these five pairs, one side of each pair, E′, did not change largely in intensity and energy, whereas the intensity of the other side, E_{LT}', increases considerably with a small change in energy at low temperatures. These results indicate that these additional

peaks are not those that were split from the E′ modes. Therefore, the 3-fold axis is not broken below T_s.

4. Discussion

4.1 Structure below T_s

Below T_s, 23 additional peaks were found. Since 14 Raman inactive modes are known to exist, we would need to consider a super-lattice structure or splitting of doubly degenerate E′ and E″ modes, to explain the number of additional peaks. We have already concluded that the additional peaks are not produced as a result of the degenerated peaks being split. Therefore, a super-lattice structure must be considered to exist below T_s.

We consider the symmetries of the point group $\bar{6}2$m below T_s. The 3-fold axis has been confirmed by the degeneracy of E′ and E″, and the polarization dependence suggested that $\bar{6}$ was not broken. The existence of the 2-fold axis along the a-axis and the mirror plane perpendicular to the a-axis cannot be discussed on the basis of the present results. Therefore, two possible point groups exist below T_s: $\bar{6}$ or $\bar{6}2$m. We would need to consider structures with $\bar{6}$, because these structures include those with $\bar{6}2$m. In the point group $\bar{6}$, the A_2' modes become Raman active. They are observed in the (c,c) and (b^*,b^*) geometries as A_1' modes. Selected additional peaks, A'_{1LT} and E'_{LT}, are likely to be A_2' modes, although this assignment cannot be made unambiguously based on the present results.

To determine the structure below T_s, we would have to focus on atomic displacements of the phonon modes with a large temperature dependence below T_s. The (c,c) spectra were found to undergo large spectral changes. Therefore, we describe the atomic displacement of all A_1' modes, which are constructed from displacements in the c-plane. Based on the SO-GGA result, $A_1'(1)$ at 100 cm^{-1} is the oscillation of the Ir-O chains, and $A_1'(2)$ at 235 cm^{-1} is the oscillation of the Ca2 atoms. The other A_1' modes are the oscillations of oxygen atoms. The atomic displacements of these oxygen A_1' modes are shown in Fig. 12. The $A_1'(6)$ mode is the oscillation of the Ir-O3 and Ir-O2 bonds. The $A_1'(5)$ mode is the oscillation of the Ir-O1 and Ir-O2 bonds. The $A_1'(3)$ mode is the vibration of the O3-Ir-O3 angle, and $A_1'(4)$ is the vibration of the Ir-O1 and Ir-O2 bonds and the O3-Ir-O3 angle.

The $A'_{1LT}(6)$ mode shows large temperature dependence in addition to anomalous appearance above T_s. Its atomic displacement cannot be obtained at present; instead, the displacement will be deduced from the displacements of the other phonon modes at approximately 430 cm^{-1}. Since the structural change at T_s is very small, the energy shift near T_s is small. Actually, only the energy of the $A'_{1LT}(6)$ mode is slightly shifted. Therefore, the phonon modes

below T_s could be inferred from those of the high-temperature structure. The phonon modes of which the energy approximates 430 cm^{-1} include $A_2'(5)$ at 436 cm^{-1} in addition to $A_1'(3)$ as presented in Table II. Note that the A_2' modes can be Raman active if the point group is $\bar{6}$ at low temperatures. If $A_{1LT}'(6)$ is a A_2' mode, it will be the $A_2'(5)$ mode. The $A_2'(5)$ mode is the vibration of the Ir-O1 direction in the c-plane, as shown in Fig. 12(b). This displacement is consistent with the observed temperature dependence of both the energy and width, as described below. Hereafter, we assume that $A_{1LT}'(6)$ is the $A_2'(5)$ mode.

The phonon modes, which have a large temperature dependence below T_s, are $A_{1LT}'(6)$ at 424 cm^{-1}, $A_1'(4)$ at 525 cm^{-1}, and $A_1'(5)$ at 550 cm^{-1}. These are the oxygen vibrations. However, $A_1'(3)$ and $A_1'(6)$ do not exhibit any anomaly below T_s, although they are also oxygen vibrations. Therefore, we would have to consider a perturbation that would modify $A_1'(4)$ and $A_1'(5)$, but would not change $A_1'(3)$ and $A_1'(6)$ largely. This would be a vibration of the O1 atoms according to their displacements shown in Fig. 12. The $A_2'(5)$ mode is also the O1 vibration. This is consistent with the assumption that $A_{1LT}'(6)$ is the $A_2'(5)$ mode.

The O1 atom has the longest Ir-O bond in the IrO_6 octahedron. In addition, the distance to the nearest Ca atom is also the longest among all the oxygen atoms. Therefore, the Ir-O1 bond is easily changed by perturbations. Here, we define the local coordinates, x' and y', at the O1 atoms, as shown in Fig. 12(a). The $A_1'(4)$ and $A_1'(5)$ modes are the vibrations of the O1 atoms along the x' direction, whereas the $A_2'(5)$ mode is the vibrations along the y' direction. The line-widths of these three modes with the O1 displacements decrease at low temperatures. This suggests that structural fluctuation includes the vibration of O1, and that the structural transition is produced by a shift in O1. The energy of the $A_2'(5)$ mode changes largely, whereas those of $A_1'(4)$ and $A_1'(5)$ do not behave anomalously at T_s. This could be the explanation if the O1 atoms were to shift in the y' direction. This displacement would change the frequency of the vibration along the y' direction, $A_2'(5)$, whereas it would have a small effect on the frequency of the vibrations along the x' direction, $A_1'(4)$ and $A_1'(5)$. Therefore, the assumption that the O1 displacements occur along the y' direction and the assignment of $A_{1LT}'(6)$ to $A_2'(5)$ are consistent with the observed anomalies. This displacement breaks the 2-fold axis along the a-axis, indicating that the point group must be $\bar{6}$.

We consider the result that many peaks appear on the (b^*, b^*) and (c, c) spectra below T_s, although the (b^*, c) spectrum contains only one additional peak. As the low-temperature structure has at least the $\bar{6}$ point group, vibrations in the c-plane are found on the (b^*, b^*) and (c, c) spectra, whereas the vibrations along the c-axis are on the (b^*, c) spectrum, because of the mirror plane perpendicular to the c-axis. A polarization dependence of a number of addi-

tional peaks would indicate that the disturbance around the atoms is large in the c-plane and small along the c-axis. Based on this argument, it is plausible to consider that the super-lattice expands in the c-plane, rather than along the c-axis. We additionally examine this conclusion from another point of view. If we consider the existence of a super-lattice structure elongated along the c-axis, many of the atoms would not be located on the mirror perpendicular to the c-axis. The vibrations of these atoms would be observed on the (b^*, b^*) and (b^*, c) spectra, because the polarization dependence arises because of the mirror. As many peaks are observed on the (b^*, b^*) spectrum, we would expect many peaks on the (b^*, c) spectrum for super-lattice structures expanded to the c-axis. However, the (b^*, c) spectrum contains only one additional peak. This indicates a super-lattice expanding in the c-plane. Here, we consider two small super-lattices, since we cannot comment on the size of the super-lattice given the present result. The first is $\sqrt{3}a \times \sqrt{3}a \times c$, with super-lattice peaks at the K-points, (1/3, 1/3, 0), in a diffraction experiment. The other is $2a \times 2a \times c$, with super-lattice peaks at the M-points, (1/2,0,0).

4.2 Landau Theory with O1 Vibrations

The transition at T_s is of the second order. According to Landau theory, the order parameter of this transition must belong to a specific irreducible representation. Based on the discussion in the previous section, the order parameter can be described by a combination of the displacement of O1 along the y' direction with a non-zero wavevector $\mathbf{q}$. Here, we examine two cases with $\mathbf{q}$ at the M-point or at the K-point.

The number of freedom of O1 vibrations is three, since one direction exists along the y' direction and three O1 atoms exist in the unit cell. At the M-point, the symmetry group, the element of which transforms $\mathbf{q}$ into its equivalent $\mathbf{q}$, is isomorphic with the point group 2mm. The O1 vibrations along the y' direction can be decomposed into A_1+$2B_2$ in 2mm, where B_2 is unchanged under m_z. If we consider only structures with the $\bar{6}$ symmetry, A_1 and B_2 produce the space group of P$\bar{6}$2m and P$\bar{6}$, respectively. To proceed to the discussion, we examine the expansion of the Landau free energy by the order parameter. We need to consider three real parameters, u_1, u_2, and u_3, since there are three M-points: $\mathbf{q}_1 = (0.5, 0, 0)$, $\mathbf{q}_2 = (0, 0.5, 0)$, and $\mathbf{q}_3 = (0.5, 0.5, 0)$. If these u_i belong to A_1, then we can express the expansion up to the fourth-order terms as

$$F = \frac{1}{2}A(u_1^2 + u_2^2 + u_3^2) + \frac{1}{3}Bu_1u_2u_3 + \frac{1}{4}C(u_1^2 + u_2^2 + u_3^2)^2 + \frac{1}{4}D(u_1^2u_2^2 + u_2^2u_3^2 + u_3^2u_1^2), \qquad (2)$$

where A, B, C, and D are parameters. If $D > 0$, we obtain the solution $(u_1, u_2, u_3) = (u, 0, 0)$.

This structure has the space group C2mm. If $D < 0$, the solution can be written as $(u_1, u_2, u_3) = (u, u, u)$. This structure has the space group P$\bar{6}$2m. We may consider the latter solution to be a possible candidate below T_s. However, in the latter case, the free energy has the third-order term, which results in a first-order transition. This is inconsistent with the second-order transition indicated by the experimental result. Therefore, the low-temperature structure cannot be this P$\bar{6}$2m structure. In the case of B_2, there is no third-order term. We can write the free energy as Eq. (2) with $B = 0$. If $D > 0$, we obtain a monoclinic structure with Pm. If $D < 0$, we obtain a hexagonal structure with P$\bar{6}$. The latter possibility is consistent with the present results, and an example of the displacement pattern of the O1 atoms is shown in Fig. 13(a).

Next, we consider structures produced by displacement with a K-point. In this case, the symmetry group of $\mathbf{q}$ is isomorphic with $\bar{6}$2m. The decomposition becomes A'_2+E′. In the case of E′, we cannot form a hexagonal structure. In the case of A'_2, we could obtain a hexagonal structure with P$\bar{6}$. The Brillouin zone contains two K-points: $\mathbf{q}_{K1} = (1/3, 1/3, 0)$ and $\mathbf{q}_{K2} = (2/3, 2/3, 0)$. These are transformed into each other by time-reversal symmetry. Then, it is sufficient to use one complex order parameter u_K, where $u_{K1} = u_K$ at $\mathbf{q}_{K1}$ and $u_{K2} = u_K^*$ at $\mathbf{q}_{K2}$. The free energy expansion up to the sixth order is

$$F = \frac{1}{2}A|u_K|^2 + \frac{1}{4}B|u_K|^4 + \frac{1}{6}C|u_K|^6 + \frac{1}{6}D(u_K^6 + u_K^{6*}), \tag{3}$$

where A, B, C, and D are parameters. For both signs of D, we can obtain hexagonal structures with the same space group P$\bar{6}$. This equation does not include a third-order term. Therefore, these P$\bar{6}$ structures are candidates for the low-temperature structure. An example of displacement for $D > 0$ is shown in Fig. 13(b).

We have found two candidates with P$\bar{6}$. We examine the observed additional modes in comparison with those of SO-GGA which become Raman active in the P$\bar{6}$ structures. In the point group $\bar{6}$, the A'_2 modes become Raman active. In addition, many modes with non-zero $\mathbf{q}$ are Raman active below T_s. In the case of Fig. 13(a), the A_1 modes and the B_2 modes at the M-points become Raman active. According to the three M-points, one of the A_1 modes becomes A'_1 + E′ below T_s. The B_2 is also decomposed into A'_1 + E′. In the case of Fig. 13(b), the A'_1, A'_2, and E′ modes at the K-points become Raman active. The A'_1 and A'_2 modes become 2A′ in P$\bar{6}$, and the E′ modes become 2E′ in P$\bar{6}$. Figure 14 shows the energies of the observed additional modes and the calculated energies (SO-GGA) of the phonon modes that become Raman active in the two P$\bar{6}$ structures. All of the observed additional modes should be related to the aggregation of the A'_2 modes at the Γ-point and the A_1 and B_2 modes at the

M-points for the structure in Fig. 13(a), or that of the A_2' modes at the Γ-point and the A_1', A_2', and E′ modes at the K-points for the structure in Fig. 13(b). The number of Raman active modes is larger than that of the observed modes in both cases, and the distribution of energies is similar in both cases. Therefore, this comparison does not enable us to conclude which is more appropriate.

4.3 Charge Fluctuation of Ir

We consider a charge fluctuation of Ir and a local structural distortion. The local structural distortion will be connected to the charge fluctuation of Ir. The valence of Ir obtained from the chemical formula is $+14/3$. Since there is only one Ir site, metallic conductivity is expected. The *ab initio* calculations also show a Fermi surface.[8)] However, the experimental results show that a semiconducting state exists even above T_s. One possible explanation is that the conduction electrons are trapped by a local distortion at a specific Ir site. Above T_s, the trapped electrons are excited thermally, and local distortion is released before being reinstated again. This leads to fluctuation of the local distortion around the Ir atom, which is consistent with the appearance of $A'_{1LT}(6)$ above T_s. The transition at T_s is likely to occur when this distortion becomes coherent.

Since the interaction between Ir ions is strong along the c-axis in a Ir-O chain, this process will result in the expansion of a super-lattice structure along the c-axis. The unit cell contains three Ir-O chains which are transformed by the 3-fold axis. Since the present result shows that the 3-fold axis is conserved below T_s, the three chains are identical below T_s. If we consider a simple charge-ordered state in the chains as Ir^{+4}-Ir^{+5}-Ir^{+5}, the smallest size of super-lattice structures is $a \times a \times 3c$. Considering the Coulombic interaction between the Ir ions, the Ir^{+4} ions would not be located on the same c-plane. This would lead to the structure with the space group $P3_121$, where the Ir^{+4} ions in each chain are shifted along the c-axis by $1/3$, according to the 3_1 screw axis. However, this structure would break the $\bar{6}$ symmetry. A structure with a $a \times a \times 3c$ superlattice and with $\bar{6}$ symmetry would have the $P\bar{6}2m$ space group or $P\bar{6}$, where all Ir^{+4} ions are located at the same z position in the unit cell. However, these structures with the elongated c-axis would not be able to explain the result that (b^*, c) only has one additional peak, as discussed above. On the other hand, if we considered the superlattice structure to expand in the c-plane, there is only one Ir atom in a chain in the primitive cell. Therefore, the Ir atoms in an individual chain are crystallographically identical in these structures. In these structures, it is difficult to explain the local distortion in a chain. As a possible state, local distortions would be randomly frozen in the chain such that the averaged structure would

have a homogeneous chain along the c-axis. According to this state, another mechanism is required to establish the structural transition at T_s.

From the point of view of a local distortion, it is worthwhile to discuss the fluctuation of the O3 atom, which is connected to one Ir atom, whereas the O1 and O2 atoms are shared by two Ir atoms. Displacement of the O3 atom therefore affects one Ir atom. This effect would be localized on one Ir site in the Ir-O chain. As seen in sec. 3.6, $A'_{1LT}(6)$ at approximately 420 cm^{-1} was observed even above T_s, which is a feature of local vibrations. The energy of $A'_{1LT}(6)$ is close to that of the $A'_1(3)$ mode, which is an angular vibration of local Ir-O3 bonds. Therefore, we could consider $A'_{1LT}(6)$ as a O3 vibration. Then, the local nature of the $A'_{1LT}(6)$ mode is consistent with that of O3. However, some observations are inconsistent with the fluctuation of the Ir-O3 directions. The fluctuation would affect the energy of $A'_1(3)$, because $A'_1(3)$ is the vibration of the Ir-O3 directions. There is no anomaly in the energy of $A'_1(3)$. In addition, the line-width of the O3 vibrational modes will be influenced by the fluctuation. The width of $A'_1(6)$, which includes the O3 vibration, shows no anomaly. Therefore, a displacement of the O3 atom would not be important for the transition at T_s and for the local distortion.

If we focus on a local fluctuation and a charge fluctuation, it would be a natural conclusion that structural change is mainly caused by O3 displacements and that the unit cell is expanded along the c-axis. However, the present result suggests another possibility. The important structural change is an O1 displacement along the y' direction. This can explain many observed anomalies. The unit cell is expanded in the c-plane. This can explain the appearance of the additional peaks. The relation of these conclusions to the charge fluctuation of Ir ions is vague at present. Moreover, the Raman scattering result cannot determine the size of the super-lattice structure. Other experiments are required to clarify the superstructures and oxygen displacements suggested above. Since the results show that local distortions exist, measurements capable of probing local structures, such as NMR measurements, would be worthwhile. Detailed measurements of the Raman scattering below the magnetic transition temperature, 7.8 K, would be interesting to estimate the interaction between the lattice and the magnetic order, because SOI is strong in $Ca_5Ir_3O_{12}$. Although the differences between 4 K and 20 K (shown in Figs. 8 and 9) are small, this would have to be investigated in future.

5. Conclusions

The Raman spectra of $Ca_5Ir_3O_{12}$ were measured from 4 K to room temperature. Using the room-temperature spectra, we assigned $6A'_1 + 9\,E' + 5E''$ among the Raman active modes,

$6A_1' + 13E' + 6E''$. The result at room temperature is consistent with the reported structure. The *ab initio* calculations of the energies of the phonon modes were performed with and without spin-orbit interaction (SOI). Both of these results agree well with the observed results.

Below the transition temperature T_s, 23 additional peaks were detected. This is clear evidence of a structural distortion below T_s. Among the additional peaks, at least one peak was observed at approximately 420 cm^{-1} even above T_s. This peak broadens and weakens with increasing temperature. This result suggests that local distortion exists above T_s. This local distortion is an important factor that could affect the semiconducting conductivity of $Ca_5Ir_3O_{12}$. We consider the displacements of O1 and O3. The O3 displacement modifies only one Ir ion and could explain local fluctuation accompanied with charge fluctuation of the Ir ions, although it is inconsistent with the observed anomalies of the energy and width. On the other hand, O1 displacements are found in the phonon modes which show anomalies in their energy and width. Therefore, these anomalies suggest that a displacement of O1 perpendicular to the Ir-O1 bond in the c-plane plays an important role in the structural change.

The additional peaks can be classified into three representations in the same way as for $\bar{6}2m$. This observation suggests the existence of $\bar{6}$ below T_s. Moreover, we confirmed the 3-fold axis below T_s because of the absence of splitting of the doubly degenerated E' and E'' modes. To explain the large number of additional peaks, a super-lattice structure is required below T_s. The existence of local distortions and the assumption of charge order fluctuation led us to suggest the existence of a $a \times a \times 3c$ super-lattice. However, this structure cannot explain the observation that 22 additional peaks were observed on the (c, c) or (b^*, b^*) spectra, whereas only one peak was found on the (b^*, c) spectrum. Another possible explanation would be the expansion of the unit cell in the c-plane. According to Landau theory, two possible structures would have the space group $P\bar{6}$. The present result is evidential of a local distortion and superlattice structure, even though the actual structural change remains unclear. Further experiments to investigate the local structures and possible superlattices would be worthwhile to perform.

Acknowledgement

We would like to thank Yoshihide Yoshimoto for useful discussions. The single crystal growth was supported by the ISSP Joint-Research program. This work is supported by a grant of the Kyushu Institute of Technology for research collaboration with other universities through utilization of research facilities, and the Promotion Project Uniting Strategic Program

of the Kyushu Institute of Technology. This research was supported by JSPS KAKENHI Grant Number JP18H04327. This research was partly supported by MEXT KAKENHI Grant Number JP15H03692. KN acknowledges support by Grants-in-Aid for Scientific Research (No.16K05452, 16H06345, 17H03379, 17H03393) from MEXT, Japan. Figures 1 and 12 were drawn by VICS-II, which was developed by Koichi Momma and Fujio Izumi.

References

1) G. Jackeli and G. Khaliullin, Phys. Rev. Lett. **102**, 017205 (2009).
2) J. Chaloupka, G. Jackeli, and G. Khaliullin, Phys. Rev. Lett. **105**, 027204 (2010).
3) Y. Machida, S. Nakatsuji, Y. Maeno, T. Tayama, T. Sakakibara, and S. Onoda, Phys. Rev. Lett. **98**, 057203, (2007).
4) K. Matsuhira, M. Wakeshima, R. Nakanishi, T. Yamada, A. Nakamura, W. Kawano, S. Takagi, and Y. Hinatsu, J. Phys. Soc. Jpn. **76**, 043706 (2007).
5) K. Matsuhira, M. Wakeshima, Y. Hinatsu, and S. Takagi: J. Phys. Soc. Jpn. **80**, 094701 (2011).
6) B. J. Kim, Hosub Jin, S. J. Moon, J.-Y. Kim, B.-G. Park, C. S. Leem, Jaejun Yu, T. W. Noh, C. Kim, S.-J. Oh, J.-H. Park, V. Durairaj, G. Cao, and E. Rotenberg, Phys. Rev. Lett. **101**, 076402 (2008).
7) M. Wakeshima, N. Taira, Y. Hinatsu, and Y. Ishii, Solid State Commun., **125**, 311 (2003).
8) K. Matsuhira, K. Nakamura, Y. Yasukuni, Y. Yoshimoto, D. Hirai, and Z. Hiroi, J. Phys. Soc. Jpn. **87**, 013703 (2018).
9) R.F. Sarkozy, W. Moeller, and B.L. Chamberland, J. Solid State Chem. **9**, 242 (1974).
10) G. Cao, V. Durairaj, S. Chikara, S. Parkin, and P. Schlottmann, Phys Rev. B, **75**, 134402 (2007).
11) I. Franke, P.J. Baker, S.J. Blundell, T. Lancaster, W. Hayes, F.L. Pratt, and G. Cao, Phys Rev. B, **83**, 094416 (2011).
12) J. Paul Attfield, Solid State Sciences **8**, 861 (2006).
13) E. B. Saloman and C. J. Sansonetti, J. Phys. Chem. Ref. Data **33**, 1113 (2004).
14) J. Yamauchi, M. Tsukada, S. Watanabe, and O. Sugino, Phys. Rev. B **54**, 5586 (1996).
15) D. Vanderbilt, Phys. Rev. B **41**, 7892 (1990).
16) K. Laasonen, A. Pasquarello, R. Car, C. Lee, and D. Vanderbilt, Phys. Rev. B **47**, 10142 (1993).
17) J. P. Perdew, K. Burke, and M. Ernzerhof, Phys. Rev. Lett. **77**, 3865 (1996).
18) A. Togo and I. Tanaka, Scr. Mater. **108**, 1 (2015) and references therein.
19) S. Kawano, S. Iikubo, and H. Ohtani, Mater. Trans. **59** 890 (2018).
20) S. Iikubo, K. Shimoyama, S. Kawano, M. Fujii, K. Yamamoto, M. Matsushita, T. Shinmai, Y. Higo, and H. Ohtani, AIP Advances **8**, 015008(2018).
21) R. Heid, K.-P. Bohnen, I. Yu. Sklyadneva, and E. V. Chulkov, Phys. Rev. B **81**, 174527 (2010).

Figure captions

Fig. 1. (Color online) (a)Crystal structure of $Ca_5Ir_3O_{12}$. The large, medium, and small spheres are Ca, Ir, and O atoms, respectively. (b) Crystal structure projected along the c-axis. The labels of the atomic positions and the $\bar{6}$ axis are shown. The height z of Ca1, Ca2, O1, and O2 is 0.5, and that of Ir and O3 is 0.

Fig. 2. (Color online) (a) *Ab initio* phonon dispersion with SOI in $Ca_5Ir_3O_{12}$. (b) Result without SOI. Dispersions are plotted along the high-symmetry points, where Γ=(0, 0, 0), L=(0, $b^*/2$, $c^*/2$), M=(0, $b^*/2$, 0), A=(0, 0, $c^*/2$), H=($-a^*/3$, $2b^*/3$, $c^*/2$), K=($-a^*/3$, $2b^*/3$, 0) with a^*, b^*, and c^* being basis vectors of reciprocal lattice, respectively. The phonon calculations were performed by considering the original symmetry based on the point group $\bar{6}2$m. (c) Calculated phonon density of states, where the SO-GGA result (thick red curves) is compared with the usual GGA result (thin blue curve).

Fig. 3. (Color online) (a) Raman spectra at room temperature. In (c, c), only A_1' modes are observable. The vertical bars are the calculated results of A_1' phonon energies with SOI. The triangles are those without SOI. (b) Magnified (b^*, b^*) and (b^*, c) spectra at room temperature. E′ and A_1' modes are observed on the (b^*, b^*) spectrum. E″ modes can be found on the (b^*, c) spectrum. The vertical bars (SO-GGA) and the triangles (GGA) are calculated energies of the E′ and E″ modes. The arrows indicate the energies of the A_1' modes determined from the (c, c) spectrum.

Fig. 4. (Color online) Raman spectra at 110 K. The arrows indicate the A_1', E′, and E″ modes assigned at room temperature. The Twotwo triangles areindicate the additional peaks which are observed above T_s. The assignment of the mode at 550 cm^{-1} is described in sec. 3.6. The vertical line at 570 cm^{-1} is intended to guide the eye guide to distinguish the $A_1'(5)$ mode at 570 cm^{-1} and the E′(11) mode at 562 cm^{-1}. The inset shows the peak at aroundapproximately 240 cm^{-1}. The vertical lines show $A_1'(2)$ and E′(4). The peak consists of these two peaks.

Fig. 5. (Color online) Raman spectra at 4 K. The modes indicated by arrows are assigned at room temperature. The additional modes found at 110 K are marked by the triangle. The vertical lines show additional modes that appear below 105 K. The small peak at 724 cm^{-1} is a natural emission line of Ne.

Fig. 6. (Color online) The dots are observed data of the (c, c) spectrum around 550 cm^{-1} at 4 K. The thick line is the result of fitting with five Lorentz peaks. The individual Lorentz peaks are also shown as dashed curves.

Fig. 7. (Color online) Temperature dependence of the (c, c) spectrum. The Lorentz curve

is that extracted for the $A'_{1LT}(6)$ mode by fitting. The arrows are A'_1 modes, and the triangles are A'_{1LT} modes, which are observed above T_s.

Fig. 8. (Color online) Temperature dependence of the energy, width, and intensity of the broad peak of $A'_{1LT}(6)$ at approximately 420 cm^{-1}. The intensity is divided by that of $A'_1(3)$ around 450 cm^{-1}. The lines are intended to guide the eye.

Fig. 9. (Color online) Temperature dependence of energy (axis on the left) and width (axis on the right) of the six A'_1 modes. The energy and width are plotted using circles and triangles, respectively. The $A'_1(4)$ and $A'_1(5)$ are estimated by five Lorentzian peaks below 110 K, or by two Lorentzian peaks above 110 K. This leads to the gaps for $A'_1(4)$ at 110 K, because of the superposition with $A'_{1LT}(9)$ at 559 cm^{-1}.

Fig. 10. (Color online) Temperature dependence of the (c, c) spectra below 110 K. The arrows indicate A'_1 modes assigned at room temperature. The triangles indicate additional peaks observed above T_s, as shown in Fig. 7. The vertical bars are additional peaks observed below T_s.

Fig. 11. (Color online) Temperature dependence of the (b^*, b^*) spectrum below 110 K. The arrows indicate A'_1 or E' modes assigned at room temperature. The vertical lines indicate additional peaks found below T_s.

Fig. 12. (Color online) (a) Projected atomic positions along the c-axis with their labels. The local coordinates, x' and y' axes, at the O1 positions are also shown. (b-f) Atomic displacements of the $A'_2(5)$ mode and four A'_1 modes obtained from the calculation with SOI. They vibrate in the c-plane.

Fig. 13. (Color online) Examples of the possible low-temperature structures described by the shift of O1 atoms along the y' direction. The shifts are indicated by the arrows. (a) The $2a\times2a\times c$ structure with $P\bar{6}$, obtained from the B_2 mode at the M-point. (b) The $\sqrt{3}a\times\sqrt{3}a\times c$ structure with $P\bar{6}$, obtained from the A'_2 mode at the K-point.

Fig. 14. (Color online) Comparison of the observed energies of the additional modes with the calculated ones. The solid circles and the solid triangles are the observed energies in the (c, c) spectrum and the $(b*, b*)$ spectrum at 4 K, respectively. The former modes are A' in $P\bar{6}$, and the latter modes are A' or E' in $P\bar{6}$. The solid squares indicate the calculated energies of the A'_2 modes, which become A' in $P\bar{6}$. The inverse solid triangles and the open squares indicate the calculated energies of the A_1 modes and the B_2 modes at the M-point, respectively. Both modes are observed as A' or E' in $P\bar{6}$. The open circles indicate the calculated energies of the A'_1 and A'_2 modes at the K-point. The open triangles indicate the calculated energies of E' at the K-point. The former become A' and the latter become E' in $P\bar{6}$.

Table I. Comparison between experimental and theoretical structural parameters of $Ca_5Ir_3O_{12}$. The experimental data are taken from Ref.[7] The SO-GGA and GGA indicate *ab initio* geometrical optimization results with and without the SOI effect, respectively.

	Expt. (120K)	SO-GGA	GGA
a [Å]	9.3490	9.3877	9.3631
c [Å]	3.1713	3.2118	3.2069
x_{Ca2}	0.7131	0.7129	0.7136
x_{Ir}	0.3334	0.3305	0.3315
x_{O1}	0.2008	0.1976	0.1992
x_{O2}	0.4620	0.4588	0.4590
x_{O3}	0.4459	0.4456	0.4458
y_{O3}	0.2407	0.2439	0.2440

Table II. Observed and calculated phonon energies in cm^{-1} unit. The obs. columns list the experimental Raman frequencies at room temperature. The SO-GGA and GGA columns are the *ab initio* results with and without SOI, respectively. Calculated results for the Raman inactive modes are also shown.

	obs.	SO-GGA	GGA		obs.	SO-GGA	GGA		SO-GGA	GGA
$A_1'(1)$	99.5	94.3	89.6	$E'(1)$	106.0	96.7	95.3	$A_1''(1)$	157.1	158.2
$A_1'(2)$	234.6	230.1	233.3	$E'(2)$	144.2	138.0	140.1	$A_1''(2)$	353.9	358.8
$A_1'(3)$	443.2	443.6	446.2	$E'(3)$		173.3	171.3	$A_2''(1)$	155.3	155.1
$A_1'(4)$	539.0	534.9	540.9	$E'(4)$	231.0	232.1	235.2	$A_2''(2)$	183.6	185.6
$A_1'(5)$	556	551.8	560.5	$E'(5)$		273.0	274.7	$A_2''(3)$	376.7	380.1
$A_1'(6)$	657.3	640.3	647.2	$E'(6)$	324.3	295.4	300.3	$A_2''(4)$	466.6	477.7
$E''(1)$	81.3	80.3	79.6	$E'(7)$		374.0	377.2	$A_2''(5)$	509.6	530.0
$E''(2)$	157.2	155.6	155.7	$E'(8)$	388.1	389.5	400.8	$A_2'(1)$	95.0	94.0
$E''(3)$	354.2	351.0	354.8	$E'(9)$	476.2	461.5	473.5	$A_2'(2)$	250.8	253.4
$E''(4)$		367.8	371.1	$E'(10)$	524	505.1	509.1	$A_2'(3)$	264.0	277.0
$E''(5)$	459.1	461.0	471.2	$E'(11)$		542.9	548.8	$A_2'(4)$	412.3	424.3
$E''(6)$	502.4	504.8	524.2	$E'(12)$	561.9	557.9	566.7	$A_2'(5)$	436.0	450.9
				$E'(13)$	615.4	620.9	625.9	$A_2'(6)$	598.4	601.3

Table III. Observed energies in cm^{-1} at 4 K. The A'_{1LT}, E'_{LT}, and E''_{LT} modes were observed in (c, c), (b^*, b^*), and (b^*, c), respectively. $A'_{1LT}(6)$ and $A'_{1LT}(9)$ were observed above 105 K.

$A'_1(1)$	100.1	$E'(4)$	235.8
$A'_1(2)$	238.2	$E'(6)$	326.9
$A'_1(3)$	448.1	$E'(7)$	390.7
$A'_1(4)$	545.2	$E'(9)$	478.0
$A'_1(5)$	574.8	$E'(10)$	520.6
$A'_1(6)$	662.2	$E'(12)$	571.0
$A'_{1LT}(1)$	194.9	$E'(13)$	625.8
$A'_{1LT}(2)$	280.6	$E'_{LT}(1)$	192.8
$A'_{1LT}(3)$	339.0	$E'_{LT}(2)$	207.6
$A'_{1LT}(4)$	384.9	$E'_{LT}(3)$	259.1
$A'_{1LT}(5)$	408.0	$E'_{LT}(4)$	269.4
$A'_{1LT}(6)$	425.5	$E'_{LT}(5)$	287
$A'_{1LT}(7)$	481.7	$E'_{LT}(6)$	333.4
$A'_{1LT}(8)$	524.6	$E'_{LT}(7)$	401.5
$A'_{1LT}(9)$	559.4	$E'_{LT}(8)$	443.6
$A'_{1LT}(10)$	588.2	$E'_{LT}(9)$	488.9
$E''(1)$	83.8	$E'_{LT}(10)$	508.7
$E''(3)$	358.0	$E'_{LT}(11)$	562.0
$E''(5)$	461.1	$E'_{LT}(12)$	659.2
$E''(6)$	510.3		
$E''_{LT}(1)$	451.3		

(a) (b)

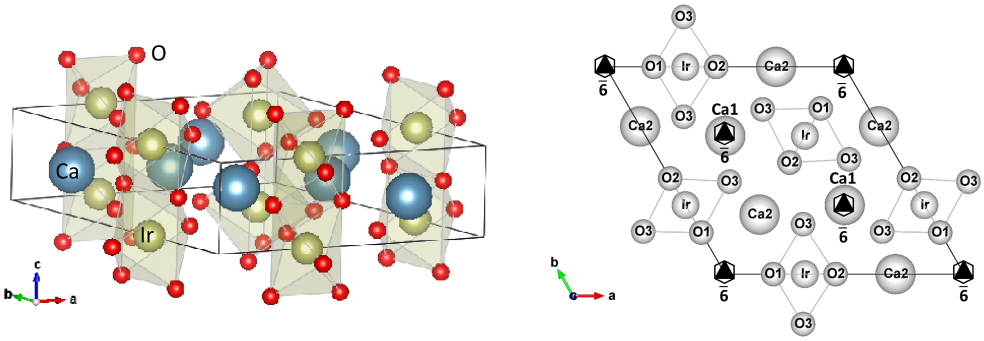

Fig. 1.

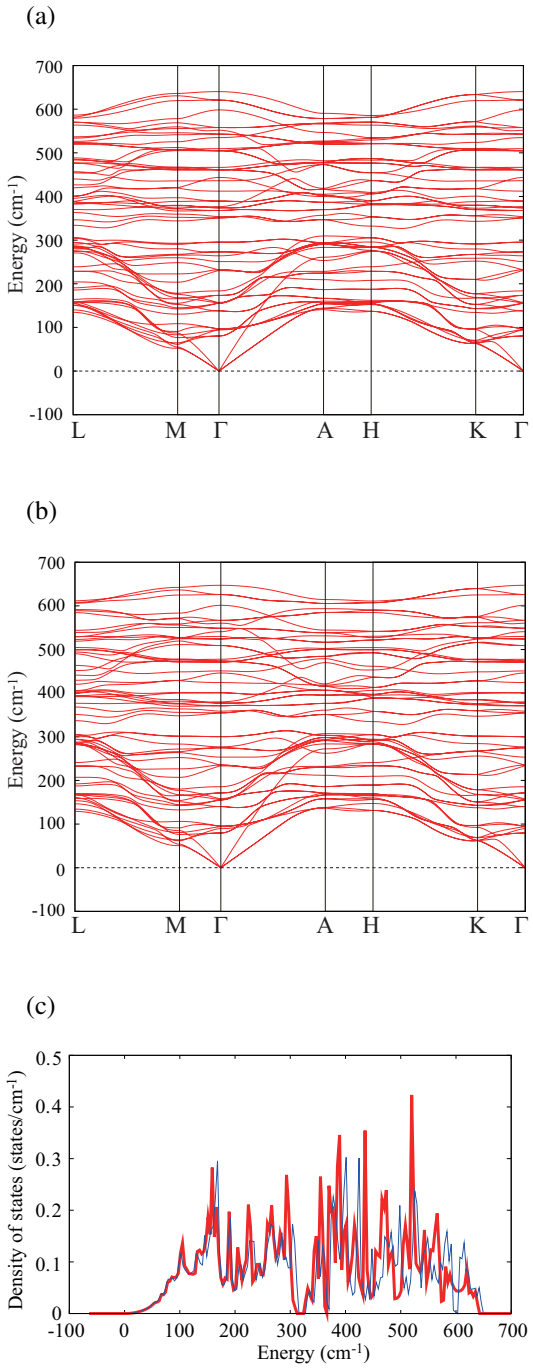
(a)
Energy (cm-1)
700
600
500
400
300
200
100
0
-100
L
M
Γ
A
H
K
Γ
(b)
Energy (cm-1)
700
600
500
400
300
200
100
0
-100
L
M
Γ
A
H
K
Γ
(c)
Density of states (states/cm-1)
0.5
0.4
0.3
0.2
0.1
0
-100
0
100
200
300
400
500
600
700
Energy (cm-1)

Fig. 2.

(a)

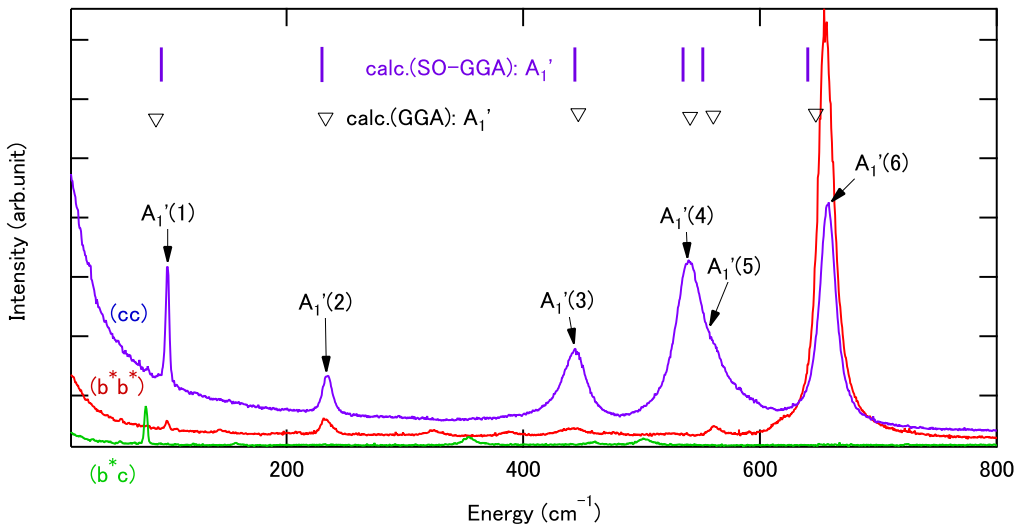
calc.(SO-GGA): A1'
calc.(GGA): A1'
A1'(1)
A1'(2)
A1'(3)
A1'(4)
A1'(5)
A1'(6)
(cc)
(b*b*)
(b*c)
Intensity (arb.unit)
Energy (cm-1)
200
400
600
800

(b)

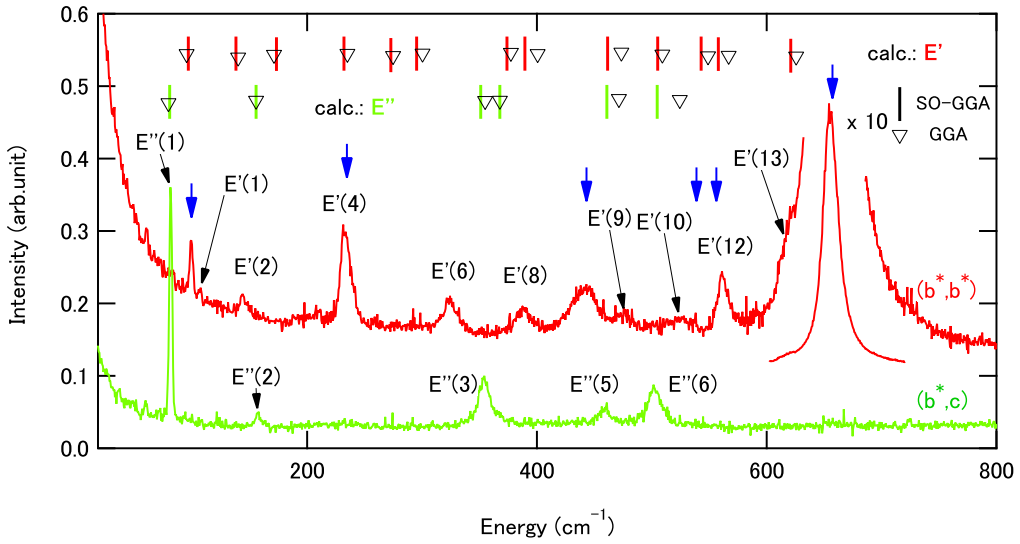
calc.: E''
calc.: E'
x 10
SO-GGA
GGA
E''(1)
E'(1)
E'(2)
E'(4)
E'(6)
E'(8)
E'(9)
E'(10)
E'(12)
E'(13)
E''(2)
E''(3)
E''(5)
E''(6)
(b*,b*)
(b*,c)
Intensity (arb.unit)
Energy (cm-1)
0.0
0.1
0.2
0.3
0.4
0.5
0.6
200
400
600
800

Fig. 3.

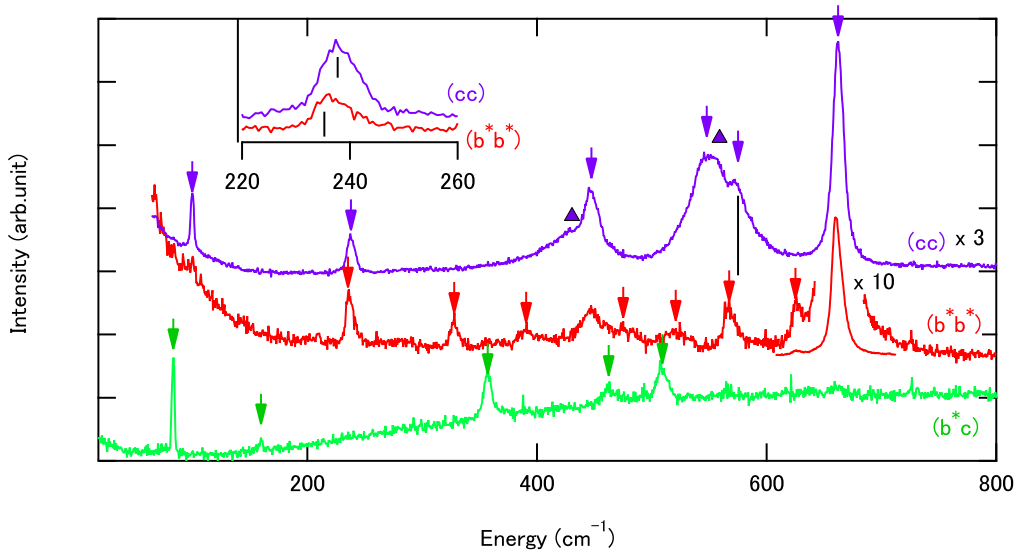
Intensity (arb.unit)
(cc)
(b*b*)
220
240
260
(cc) x 3
x 10
(b*b*)
(b*c)
200
400
600
800
Energy (cm-1)

Fig. 4.

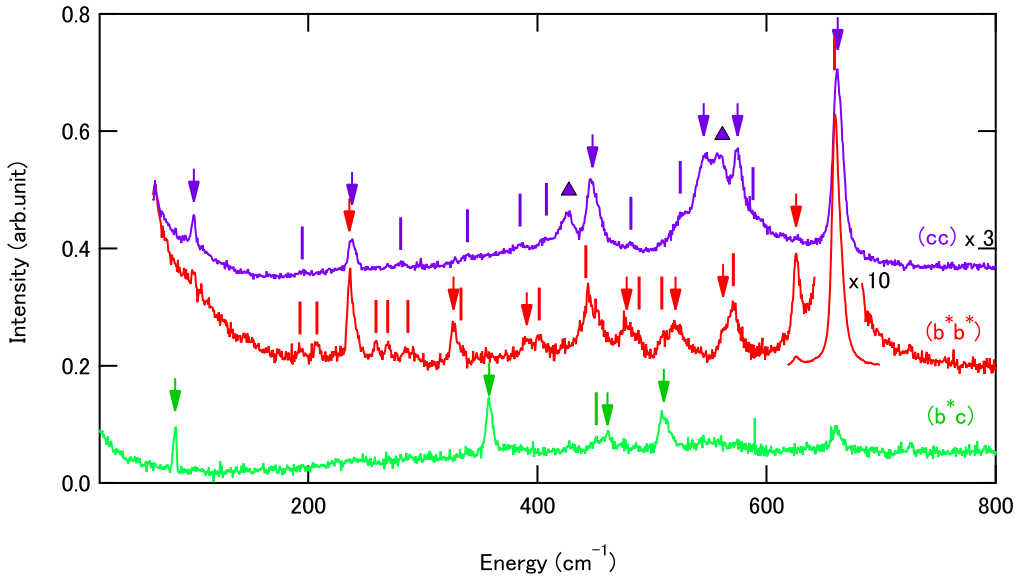
0.8
0.6
0.4
0.2
0.0
Intensity (arb.unit)
200
400
600
800
Energy (cm^{-1})
(cc) x 3
x 10
(b*b*)
(b*c)

Fig. 5.

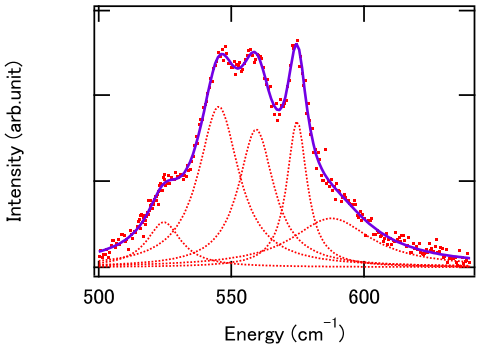

Fig. 6.

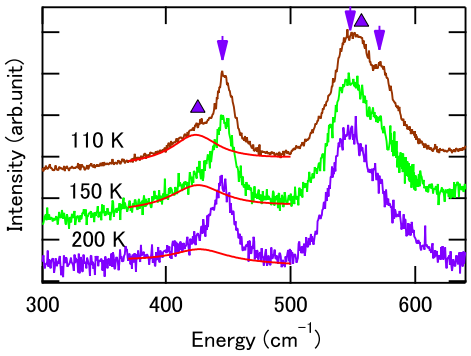

Fig. 7.

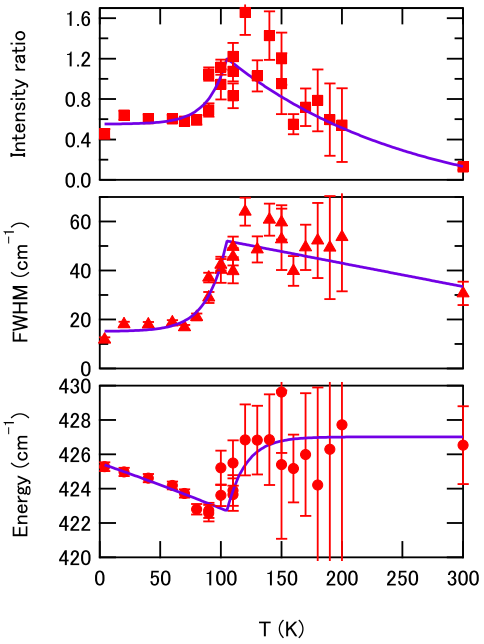
Intensity ratio
1.6
1.2
0.8
0.4
0.0
FWHM (cm^{-1})
60
40
20
0
Energy (cm^{-1})
430
428
426
424
422
420
0
50
100
150
200
250
300
T (K)

Fig. 8.

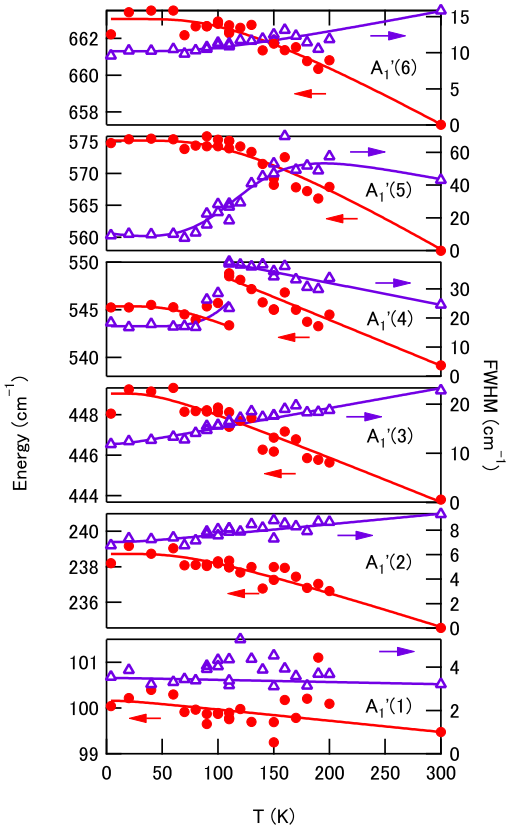
Energy (cm^{-1})
FWHM (cm^{-1})
T (K)
A$_1$'(6)
A$_1$'(5)
A$_1$'(4)
A$_1$'(3)
A$_1$'(2)
A$_1$'(1)
662
660
658
575
570
565
560
550
545
540
448
446
444
240
238
236
101
100
99
0
50
100
150
200
250
300
15
10
5
60
40
20
30
8
6
4
2

Fig. 9.

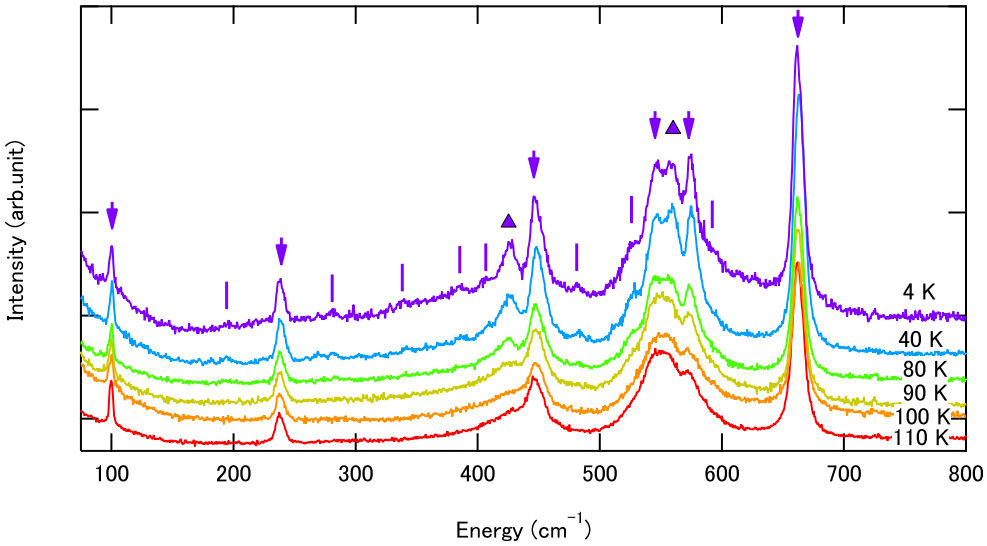
Intensity (arb.unit)
Energy (cm^{-1})
100
200
300
400
500
600
700
800
4 K
40 K
80 K
90 K
100 K
110 K

Fig. 10.

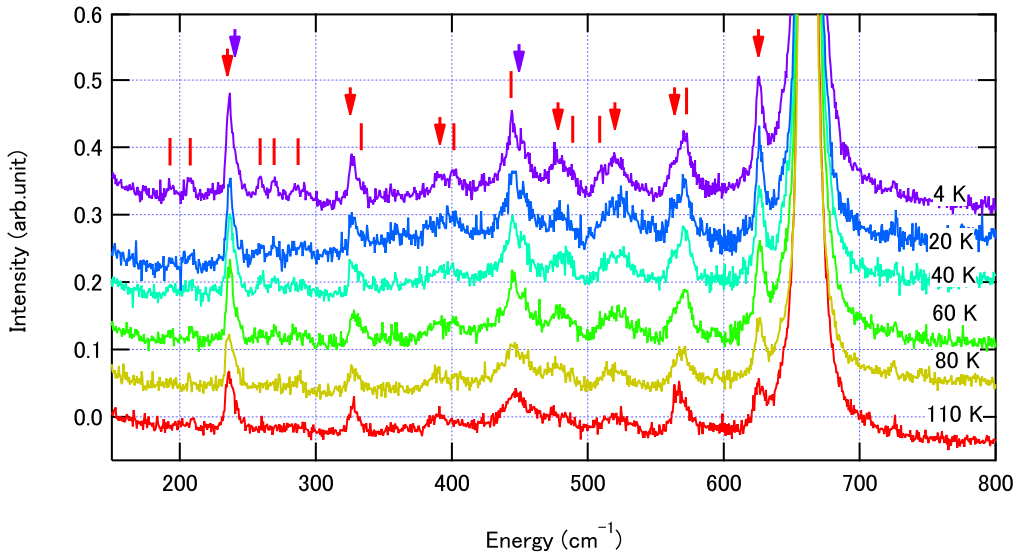
0.6
0.5
0.4
0.3
0.2
0.1
0.0
Intensity (arb.unit)
200
300
400
500
600
700
800
Energy (cm^{-1})
4 K
20 K
40 K
60 K
80 K
110 K

Fig. 11.

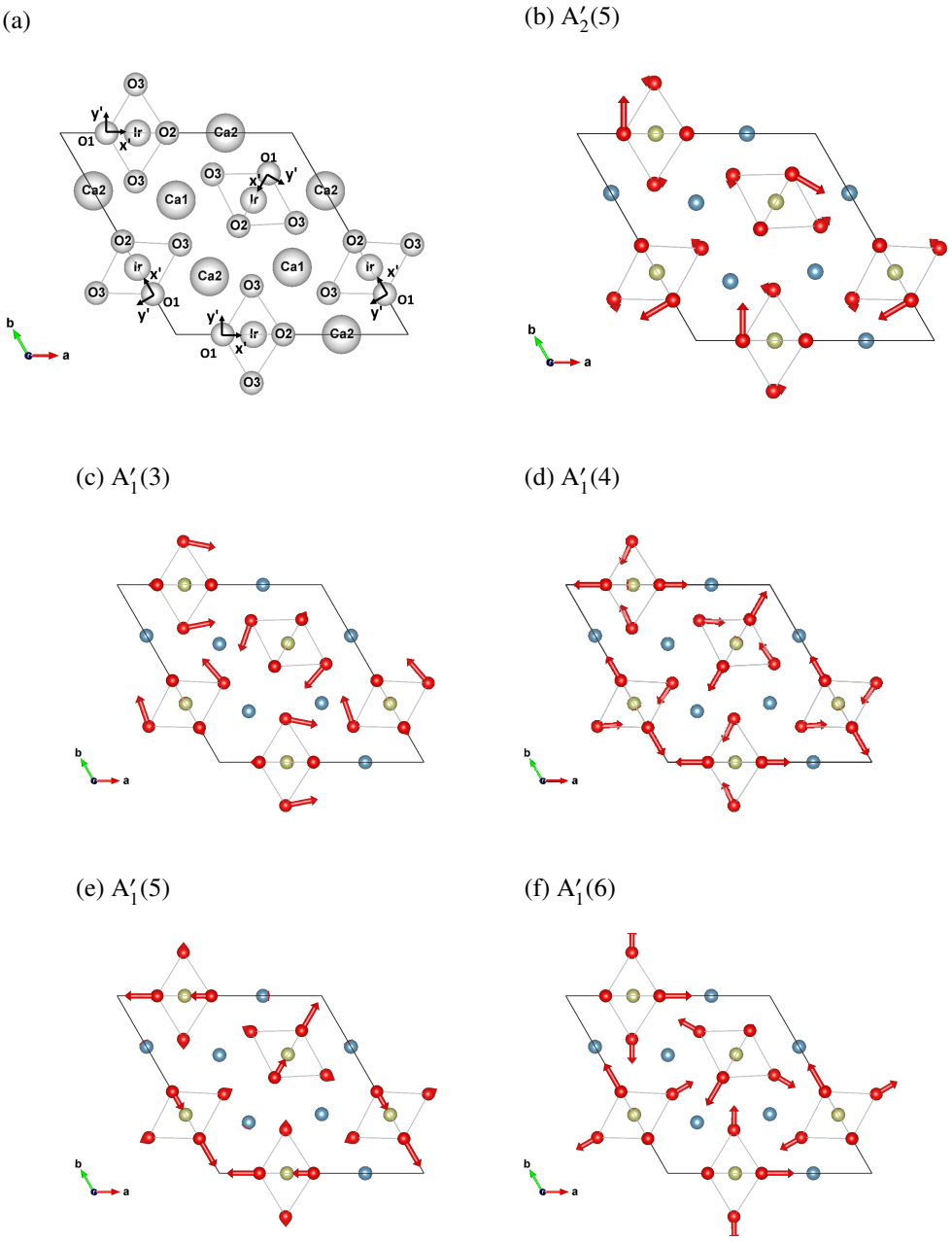

Fig. 12.

(a) M: B_2 (b) K: A_2'

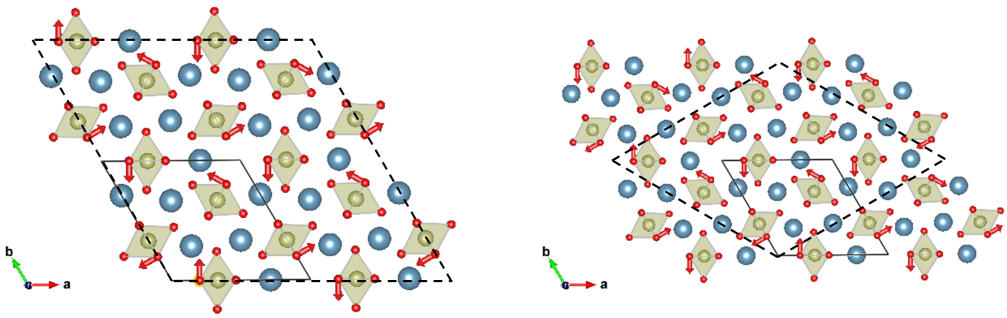

Fig. 13.

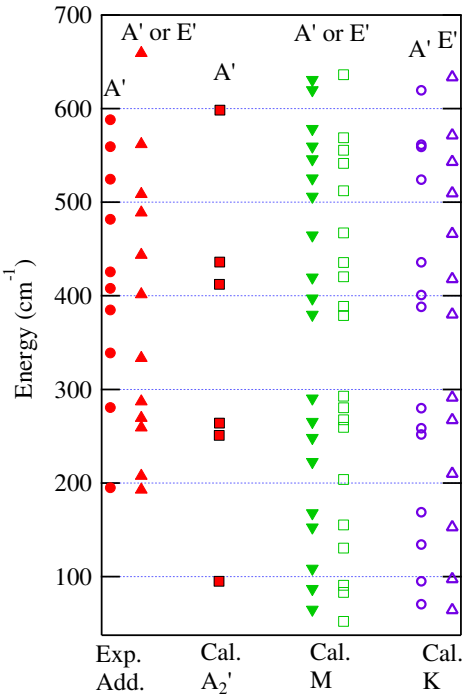
700
600
500
400
300
200
100
Energy (cm^{-1})
A' or E'
A'
A'
A' or E'
A'
E'
Exp.
Add.
Cal.
A_2'
Cal.
M
Cal.
K

Fig. 14.